This is the accepted manuscript made available via CHORUS. The article has been published as:

Cell augmentation framework for topological lattices

Mohammad Charara and Stefano Gonella

Phys. Rev. B **108**, L020301 — Published 7 July 2023

DOI: 10.1103/PhysRevB.108.L020301

A cell augmentation framework for topological lattices

Mohammad Charara[1] and Stefano Gonella[1,*]

[1] *Department of Civil, Environmental, and Geo- Engineering, University of Minnesota, Minneapolis, Minnesota 55455, USA*

Maxwell lattices are characterized by an equal number of degrees of freedom and constraints. A subset of them, dubbed topological lattices, are capable of localizing stress and deformation on opposing edges, displaying a polarized mechanical response protected by the reciprocal-space topology of their band structure. In two dimensions, the opportunities for topological polarization have been largely restricted to the kagome and square lattice benchmark configurations, due to the non-triviality of generating arbitrary geometries that abide by Maxwell conditions. In this work, we introduce a generalized family of augmented topological lattices that display full in-plane topological polarization. We explore the robustness of such polarization upon selection of different augmentation criteria, with special emphasis on augmented configurations that display dichotomous behavior with respect to their primitive counterparts. We corroborate our results via intuitive table-top experiments conducted on a lattice prototype assembled from 3D-printed mechanical links.

Mechanical metamaterials feature dynamical behavior that transcends that of conventional elastic media [1–4]. Lattice metamaterials, specifically, owe their distinctive macro-scale behavior to the periodicity of their microstructure, composed of tessellated *unit cells* [5–7]. Maxwell systems are a special class of lattices, characterized by an equal number of degrees of freedom and constraints [8–10]. They posses interesting characteristics such as reconfigurability [11–14], geometric behavioral dualities [15, 16], and, of current relevance, the ability to host zero-energy (*floppy*) modes [17–19] – where sites displace without straining the bonds.

When freed from an infinite domain by cutting certain bonds, Maxwell lattices localize zero modes at the edges due to a local imbalance between degrees of freedom and constraints [18, 19]. Certain Maxwell lattices have been shown to localize deformation and stress on opposite edges, a feature referred to as *topological polarization*, which is protected against defects by the momentum-space topology of the bulk [20–26]. This polarization manifests as an excess of zero modes at the *floppy edge*, while the opposite edge remains rigid.

Topological polarization has been discussed for lattices with one-dimensional (1D) [22, 23], 2D [14, 22, 27–32], and 3D periodicity [33–35], and, more recently, for 2D-periodic bilayers embedded in 3D space [36, 37]. However, in 2D, studies have largely been restricted to deformed configurations of the canonical square [28, 32] and kagome lattice [14, 18]. A gap exists in the study of topological lattices with increased cell geometry complexity and kinematics. Filling this gap provides a golden opportunity to search into a broader design landscape for additional topologically polarized configurations.

In this letter, we introduce a family of topological lattices whose augmented unit cells contain a higher number of sites and bonds than the kagome or square lattices. In general, the task of generating augmented unit cells adhering to Maxwell conditions is non-trivial, as configurations resulting from the process may be over- or under-coordinated. A promising path consists of leveraging known unit cells amenable to topological polarization as elementary building blocks. In this regard, here we adopt a distorted kagome cell as a primitive geometry, and augment it through a series of mirror-folding operations. We document analytically an emergent topological polarization, and explore parametrically its robustness upon changes in geometry. Although we primarily focus on single-mirror augmentation, we introduce a generalization of this approach to multi-mirror augmentation strategies; while generally not guaranteeing full polarization, these extended strategies still yield asymmetric response scenarios with an unequal number of zero modes localized at opposing edges. We validate our results via experiments on a prototype assembled from 3D-printed mechanical links.

A kagome unit cell consists of two triangles meeting at a vertex. Alternatively, it can be interpreted as three sites $\bar{\mathbf{r}}_i$ connected to each other and to adjacent cells by six bonds $\bar{\mathbf{b}}_{ij} = \bar{\mathbf{r}}_j - \bar{\mathbf{r}}_i$, taken as springs of equal stiffness. A parametric description of the unit cell shown in Fig. 1(a) is given in terms of $\bar{\mathbf{r}}_1 = [1, \Delta]$, $\bar{\mathbf{r}}_2 = [\cos(\pi/3), \sin(\pi/3)]$, and $\bar{\mathbf{r}}_3 = [0, 0]$, with lattice vectors $\bar{\ell}_1 = [2, \sin(\gamma) - \Delta]$ and $\bar{\ell}_2 = [1, \sin(\pi/3) + 0.57\sin(\pi/4 + \gamma) - \Delta]$, where γ is a parameter that rotates, counterclockwise, bonds $\bar{\mathbf{b}}_{13'} = (\bar{\mathbf{r}}_3 + \bar{\ell}_1) - \bar{\mathbf{r}}_1$ and $\bar{\mathbf{b}}_{12'} = (\bar{\mathbf{r}}_2 - \bar{\ell}_2 + \bar{\ell}_1) - \bar{\mathbf{r}}_1$, changing the length of $\bar{\mathbf{b}}_{13'}$ (translating $\bar{\mathbf{r}}_3 + \ell_2$ vertically), and Δ adjusts the vertical position of $\bar{\mathbf{r}}_1$. Starting from this, we introduce the augmented cell shown in Fig. 1(b), which we refer to as bi-kagome (BK), acquired by mirroring the kagome cell about an axis (dashed line) passing through $\bar{\mathbf{r}}_1$ and $\bar{\mathbf{r}}_3 + \bar{\ell}_2$. This geometry features six sites $\mathbf{r}_i$ and 12 bonds $\mathbf{b}_{ij} = \mathbf{r}_j - \mathbf{r}_i$ per unit cell, with periodicity over $\ell_1 = [4, 0]$ and $\ell_2 = [2, \sin(\pi/3) + 0.57\sin(\pi/4 + \gamma)]$, where $\mathbf{r}_1 = \bar{\mathbf{r}}_1$, $\mathbf{r}_2 = \bar{\mathbf{r}}_2$, $\mathbf{r}_3 = \bar{\mathbf{r}}_3$, $\mathbf{r}_4 = [2, 0]$, $\mathbf{r}_5 = \mathbf{r}_2 + [1, 0]$,

* sgonella@umn.edu

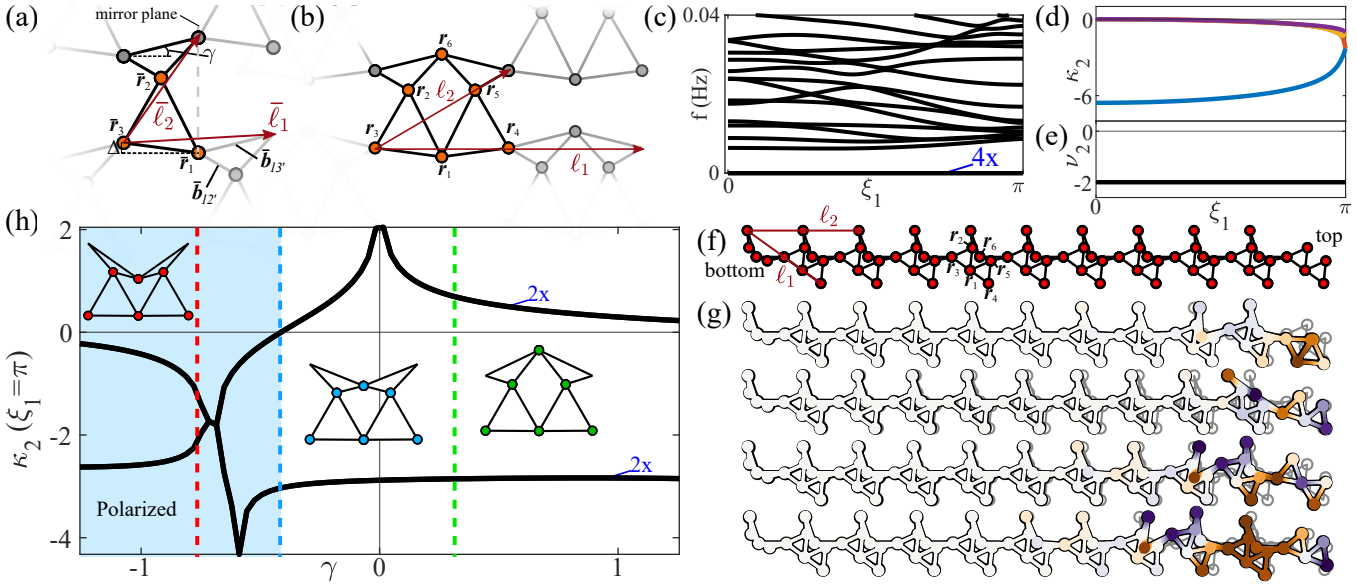


FIG. 1. (a) Kagome (SK) and (b) bi-kagome (BK) unit cells, where orange sites belong to the unit cell and gray sites belong to adjacent unit cells; (c) supercell band diagram for the BK unit cell with $\gamma = -\pi/4$, featuring four zero modes, and (d) decay rate κ_2 of zero modes and (e) winding number ν_2 across the Brillouin Zone (BZ). (f) Supercell geometry and (g) mode shapes of the edge-localized zero modes at $\xi_1 = \pi$. (h) κ_2 at $\xi_1 = \pi$, as a function of γ, with examples of fully polarized (red), non-polarized (green), and phase transition (blue) configurations.

$\mathbf{r}_6 = [1, \sin(\pi/3) + 0.57\sin(\pi/4 - \gamma) + \sin(\gamma)]$. For clarity, henceforth we refer to the primitive kagome as single kagome (SK). Within the available landscape of augmentation and parametrization techniques, the current method is chosen as only one of the BK lattice vectors is dependent on γ. In this work, for convenience, we fix $\Delta = -0.03$, reducing the parameter space to just γ (details about the effects of varying the parameter Δ can be found in the Supplemental Materials (SM) [38]).

We investigate the polarization of the augmented cell by adapting a general framework for Maxwell lattices [19]. The compatibility matrix $\mathbf{C}$ of a cell relates site displacements $\mathbf{U}$ to bond elongations $\mathbf{E}$. Maxwell lattices can experience zero-energy modes that displace the sites without deforming the bonds (i.e. $\mathbf{CU} = 0$), therefore spanning the nullspace of $\mathbf{C}$, under appropriate boundary conditions. These zero modes can manifest in the bulk or localize to an edge. The topological polarization of a lattice is marked by an excess of zero modes localized on a certain edge. Focusing on the benchmark BK configuration with $\gamma = -\pi/4$, we confirm the emergence of zero modes by studying the supercell shown in Fig. 1(f), encompassing 10 cells along ℓ_2, with Bloch-periodic boundary conditions along ℓ_1 and free boundary conditions at the top and bottom edges. Indeed, the resulting supercell band diagram (Fig. 1(c)) features four overlapping zero modes. Their four corresponding mode shapes at $\xi_1 = \pi$, shown in Fig. 1(g), indicate that *all* four are edge modes localized on the top edge, denoting *full polarization*. Note that although in the current work we explore polarization in the ℓ_2 direction, the same treatment can be taken for ℓ_1 (see SM for these details [38]).

The degree of localization of a mode is characterized by its decay rate into the bulk κ_2 [along ℓ_2], calculated for each transverse wave number ξ_1, sampled along ℓ_1, using the procedure described in Ref. [37] (see SM for details on calculations of zero mode decay rates). Decay rates calculated across the BZ for $\gamma = -\pi/4$ are shown in Fig. 1(d), where $\kappa_2 < 0$ (> 0) denotes zero modes localized at the top (bottom) edge. The four zero modes are, indeed, localized on the top edge. Polarization along ℓ_2 is protected by the topological invariant integer *winding number* ν_2, calculated for each wavenumber ξ_1 over a closed loop in the BZ [22] (see SM for winding number calculation). As shown in Fig. 1(e), $\nu_2 = -2$ for all wavenumbers; this captures a transition [with respect to the ground state] of two zero modes from the stiff edge to the floppy edge, rendering the configuration fully polarized, and validates the topological roots of the observed behavior.

Focusing on the short-wavelength limit ($\xi_1 = \pi$), we study the dependence of the degree of localization of the modes (and therefore polarization of the lattice) – embodied by κ_2 – on the parameter γ. The sweep $\gamma = [-\pi/2.5\ \pi/2.5]$ is shown in Fig. 1(h). For all values of γ, the decay rate curves are doubly degenerate (becoming quadruple degenerate locally around $\gamma = -\pi/6$), indicating that there exists, in general, two distinct decay patterns allowed by the lattice. Importantly, for configurations with $\gamma < -0.4135$, the lattice displays full po-

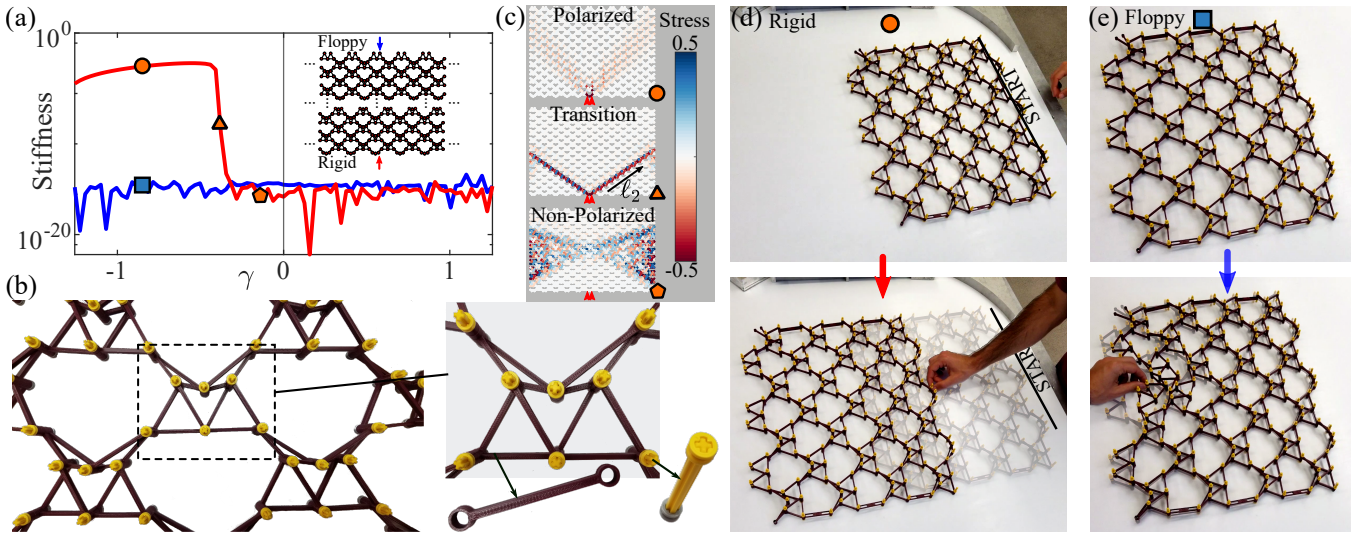


FIG. 2. (a) Edge stiffness values, as a function of γ, inferred via full-scale static simulations of an 81×81 BK lattice probed by a point load with the red (blue) curve referring to the rigid (floppy) edge. (b) Detail of the lattice with a close-up of an individual BK unit cell, a 3D-printed link, and the Lego® axles and bushings used as hinges. (c) Snapshots of stress concentration on an 11×11 lattice for a polarized, phase transition, and nonpolarized configurations with loading at the rigid edge. Quasi-static experiments performed loading from the rigid (d) and floppy (e) edges, yielding rigid-body motion and displacement localization, respectively (see video of experiments in SM [38]).

larization, with all four zero modes localized on the top edge.

We quantify the asymmetry of the static response of the lattice by performing full-scale static simulations of an 81×81-cell domain, loaded by a unit-amplitude force applied at the midpoint of the top (bottom) edge while constraining the other edges. We infer edge stiffness by dividing the applied force by the resulting displacement on the loaded point. We repeat this exercise for the range $\gamma = [-\pi/2.5\ \pi/2.5]$, with the stiffness of the rigid (floppy) edge shown in red (blue) in Fig. 2(a). For low γ values, the large gap between the two curves denotes asymmetric edge stiffness: the floppy edge features essentially zero stiffness (within computational error), while the stiff edge value is finite. At $\gamma > -0.4135$, the stiffness curves coalesce, marking the transition to a nonpolarized regime. The effects of a geometry sweep on the topological phase have been discussed in Ref. [14] for a deformed kagome lattice, where the bounds of polarization were identified as the twist angles between the triangles for which their edges align to form states of self-stress (SSS). Here, the same condition cannot be met by the BK lattice due to the impossibility to form straight lines of bonds for all γ. However, a qualitative rationale for the driver of phase transition can be inferred by studying the stress concentration patterns developing in the lattice in different regimes. Snapshots of static simulations of an 11×11 lattice loaded by a force applied at the rigid edge, shown in Fig. 2(c), reveal that, for a configuration at the phase transition point, *force chains* develop from the loading point into the bulk along ℓ_2, playing a role akin to an SSS. In stark contrast, a polarized configuration develops stress concentration at the rigid edge, decaying into the bulk, while for a nonpolarized configuration, stress concentration patterns emanate from the lateral boundaries.

We construct a mechanical prototype resembling the ideal spring-mass system used in our theoretical predictions, with slender links 3D-printed (Prusa MK3S) out of polylactic acid (PLA) and connected with nearly frictionless rod-like hinges of Lego® axles and bushings. The assembled 5×8 lattice is shown in Fig. 2(b), where the nonperiodic bonds at the left and right boundaries help eliminate trivial floppy behavior of dangling bonds. Figs. 2(d) and (e) show the behavior of the lattice when quasi-statically manually loaded from the rigid and floppy edges, respectively. When pushed from the floppy edge, the lattice responds by developing a soft mode that localizes at the floppy edge, eventually morphing into geometrically non-linear deformation, involving macroscopic rotations of the triangles, that decays sharply into the bulk. Note that topological polarization theory, which is strictly linear, predicts only the softness of an edge and not the nonlinear deformation regime that unfolds. In contrast, loading from the rigid edge results in rigid body motion of the entire lattice.

To showcase the richness of strategies for cell augmentation available within the proposed framework, we consider an alternative variant of the BK lattice, which, remarkably, can display polarization when its SK counterpart is unpolarized. Take the SK lattice and its BK counterpart in Fig.s 3(a) and (b), respectively (see SM

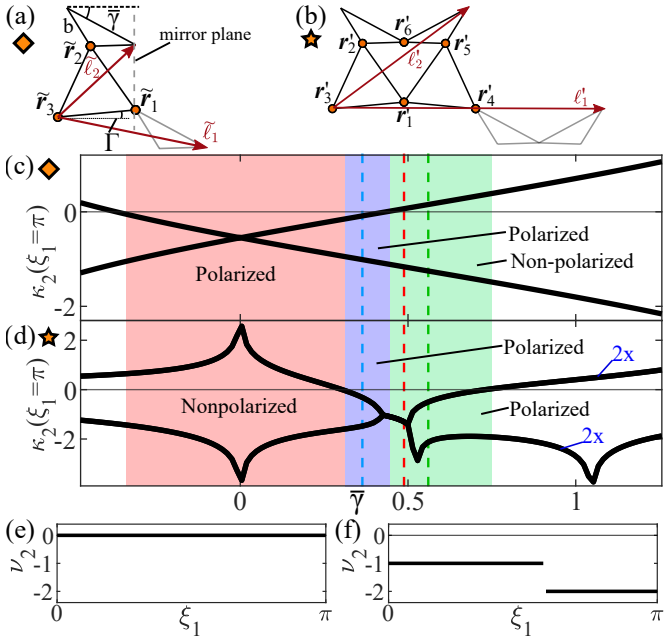


FIG. 3. (a) SK and (b) BK unit cells parametrized in terms of the twist angle $\bar{\gamma}$. $\kappa_2(\xi_1 = \pi)$ for the (c) SK and (d) BK in the interval $\bar{\gamma} = [-\pi/6.6\ \pi/2.5]$, where the red (green) shading highlights parameter regions where the SK (BK) is fully polarized while the BK (SK) is not, and the blue region highlights parameters where both geometries are polarized; winding number ν_2 of the (e) SK and (f) BK lattices for an example case (green dotted line).

for details about $\bar{\gamma}$ BK parametrization). Following the procedure above, we calculate the κ_2 for the SK and BK unit cells over the parameter space $\bar{\gamma} = [-\pi/6.6\ \pi/2.5]$, and plot the results for $\xi_1 = \pi$ in Fig. 3(c) and (d), respectively. The green region denotes a parameter range in which the BK lattice is polarized while its SK counterpart is not, and the red region exhibits the opposite trend, with the SK polarized and the BK nonpolarized. In the blue region, both lattices display polarization. As an example, winding number ν_2 calculations for $\bar{\gamma} = 0.57$ (green dotted line) for the SK (Fig. 3(e)) and BK (Fig. 3(f)) elucidate their topological dichotomy. For the SK lattice $\nu_2 = 0$, indicating no polarization, while for the BK $\nu_2 = -2$ for shorter wavelengths and $\nu_2 = -1$ for longer wavelengths, both signaling topological polarization, albeit with differing strengths. The integer change observed in ν_2 is a well documented occurrence associated with the existence of a *Weyl point* in the bulk band diagram, which denotes the existence of bulk zero modes [28, 35].

The versatility of the cell augmentation framework can be appreciated by considering a generalization of the process involving multiple mirroring steps preceding cell tessellation, resulting in additional proliferation of sites and bonds in each unit cell. For example, Fig. 4(a) shows a unit cell generated by further mirroring the BK unit cell from Fig. 1(a) about sites $\mathbf{r}_4$ and $\mathbf{r}_3 + \ell_2$ (the latter becoming $\mathbf{r}_9$ after mirroring). In principle, the process can involve an arbitrary number of horizontal mirroring operations; we introduce label T_h denoting the number of BK units assembled along the ℓ_1 direction in the augmented cell. Fig.s 4(b), (d), and (f) show three examples ranging from $T_h = 1$ (original BK) to $T_h = 3$. The modal displacement U_{n_2}, defined as the magnitude of the site displacements in each cell of a given supercell modeshape, allows for qualitative visualization of the decay into the bulk of that mode. We plot U_{n_2} for the considered configurations in Fig. 4(c), (e), and (g), respectively, using a 20-cell supercell, where $n_2 = 1$ ($n_2 = 20$) denotes the bottom (top) edge. Interestingly, in the bulk, for $T_h > 1$ the trend of localization towards the top edge persists, signaling robustness of the polarization against the augmentation process. However, most modes also display a sharp increase in displacement localized strictly to the last unit cell on the bottom edge. For augmented cells, this trivial edge effect may overwhelm the edge-selective attribute of the bulk that is ascribable to topological pro-

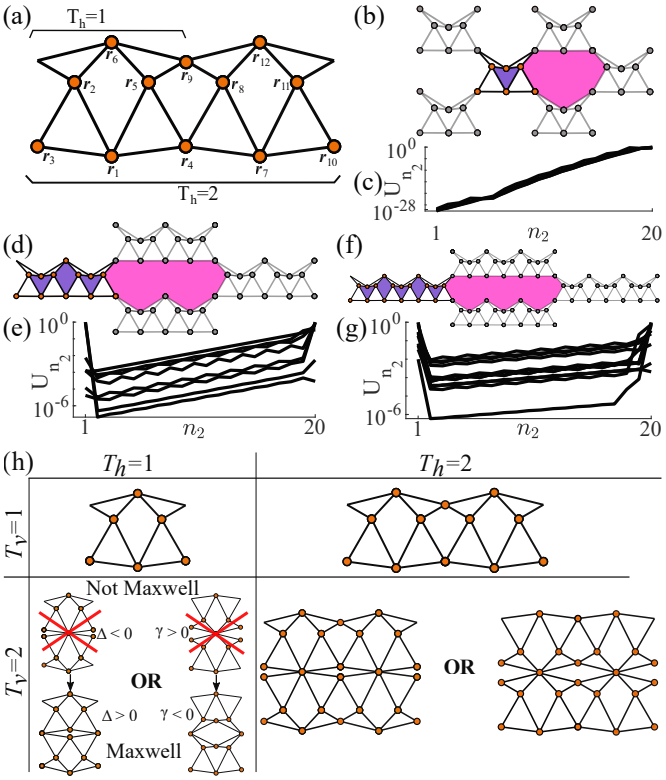


FIG. 4. (a) Example of augmented unit cell featuring two connected BK unit cells (i.e. $T_h = 2$). Truncated lattices for (b) $T_h = 1$, (d) $T_h = 2$, and (f) $T_h = 3$, highlighting emergent void polygons, and their modal displacement U_{n_2} (c, e, g, respectively) plotted as a function of the unit cell index for all supercell zero modes. (h) Sample augmentation strategies with $T_h = 1, 2$ and $T_v = 1, 2$, where the $T_v = 2$ row depicts augmentation via two distinct mirroring operations about the ℓ_1 axis.

tection.

Further, it can be shown that, despite profound changes in geometry induced by varying T_h, the effective spatial density of the lattice remains constant (see SM for details of density calculation). This implies that we can sweep the structural design landscape of the lattice via cell augmentation, tuning the polarization, without changing the effective weight, which is often a major constraint in structural design. However, the augmentation process exacerbates the degree of heterogeneity of the lattice: as T_h increases, the number of purple quadrilaterals follows T_h+1 and the number of edges of the pink polygonal gaps is $4+4T_h$. This trend progressively localizes the solid phase of the lattice, while introducing (and progressively stretching) a length scale (i.e., ℓ_i) associated with periodicity of the augmented cell (with interesting implications on bulk phonons – see Supplemental Material for related band diagrams).

Finally, mirroring is not restricted to the ℓ_1 direction; in fact, we can also introduce T_v vertical mirrors (in the $\ell_2+\ell_1/2$ direction), or even T_d diagonal mirrors (see SM for example geometry). Fig. 4(h) tabulates unit cells generated for $T_h = 1, 2$ and $T_v = 1, 2$, where the row $T_v = 2$ displays two alternative mirroring strategies. Frame ($T_h = 1$ - $T_v = 2$) highlights that this augmentation strategy should be handled with care as certain Δ and γ ranges may result in non-Maxwell lattices. The same two vertical mirroring strategies are shown for ($T_h = 2$ - $T_v = 2$), where the resulting lattices are still Maxwell by considering the *average* count of sites and bonds over the cell, while accepting that certain sites will be under- and over- coordinated. Validating the topological nature of such resulting configurations requires future investigation (see SM for sample geometries).

In summary, we introduce a family of augmented Maxwell lattices obtained through mirror operations performed on kagome cells, which display full polarization. The mirror-folding strategy introduced is merely a small subset of a larger landscape of super-geometries that can be generated with the framework. This process begins to uncover a larger dimensional space for topological lattices, with implications on the versatility of this geometry class for structural design.

This work is supported by the National Science Foundation (Grant No. EFRI-1741618). We acknowledge the support of the UMN Clifford I. and Nancy C. Anderson Student Innovation Labs and are grateful to James McInerney for the many insightful discussions.

[1] S. Babaee, J. Shim, J. C. Weaver, E. R. Chen, N. Patel, and K. Bertoldi, Advanced Materials **25**, 5044 (2013).
[2] A. Rafsanjani and D. Pasini, Extreme Mechanics Letters **9**, 291 (2016).
[3] A. S. Meeussen, E. C. Oğuz, Y. Shokef, and M. v. Hecke, Nature Physics **16**, 307 (2020).
[4] W. Zunker and S. Gonella, Extreme Mechanics Letters **46**, 101344 (2021).
[5] L. Brillouin, *Wave propagation in periodic structures: electric filters and crystal lattices*, Vol. 2 (Dover publications, 1953).
[6] A. S. Phani, J. Woodhouse, and N. Fleck, The Journal of the Acoustical Society of America **119**, 1995 (2006).
[7] C. Widstrand, N. Kalantar, and S. Gonella, Extreme Mechanics Letters **53**, 101693 (2022).
[8] J. C. Maxwell, The London, Edinburgh, and Dublin Philosophical Magazine and Journal of Science **27**, 294 (1864).
[9] C. R. Calladine, International journal of solids and structures **14**, 161 (1978).
[10] S. Pellegrino and C. R. Calladine, International Journal of Solids and Structures **22**, 409 (1986).
[11] S. Guest and J. Hutchinson, Journal of the Mechanics and Physics of Solids **51**, 383 (2003).
[12] K. Sun, A. Souslov, X. Mao, and T. Lubensky, Proceedings of the National Academy of Sciences **109**, 12369 (2012).
[13] X. Mao, O. Stenull, and T. C. Lubensky, Physical Review E **87**, 042601 (2013).
[14] D. Rocklin, S. Zhou, K. Sun, and X. Mao, Nature communications **8**, 1 (2017).
[15] S. Gonella, Phys. Rev. B **102**, 140301 (2020).
[16] M. Fruchart, Y. Zhou, and V. Vitelli, Nature **577**, 636 (2020).
[17] S. Pellegrino, International Journal of Solids and Structures **30**, 3025 (1993).
[18] T. Lubensky, C. Kane, X. Mao, A. Souslov, and K. Sun, Reports on Progress in Physics **78**, 073901 (2015).
[19] X. Mao and T. C. Lubensky, Annual Review of Condensed Matter Physics **9**, 413 (2018).
[20] M. Z. Hasan and C. L. Kane, Reviews of modern physics **82**, 3045 (2010).
[21] X.-L. Qi and S.-C. Zhang, Reviews of Modern Physics **83**, 1057 (2011).
[22] C. Kane and T. Lubensky, Nature Physics **10**, 39 (2014).
[23] B. G.-g. Chen, N. Upadhyaya, and V. Vitelli, Proceedings of the National Academy of Sciences **111**, 13004 (2014).
[24] J. Paulose, B. G.-g. Chen, and V. Vitelli, Nature Physics **11**, 153 (2015).
[25] X. Li, S. Yu, H. Liu, M. Lu, and Y. Chen, Current Opinion in Solid State and Materials Science **24**, 100853 (2020).
[26] C. Widstrand, C. Hu, X. Mao, J. Labuz, and S. Gonella, arXiv preprint arXiv:2209.14463 (2022).
[27] J. Paulose, A. S. Meeussen, and V. Vitelli, Proceedings of the National Academy of Sciences **112**, 7639 (2015).
[28] D. Z. Rocklin, B. G.-g. Chen, M. Falk, V. Vitelli, and T. Lubensky, Physical review letters **116**, 135503 (2016).
[29] J. Ma, D. Zhou, K. Sun, X. Mao, and S. Gonella, Physical review letters **121**, 094301 (2018).
[30] O. Stenull and T. Lubensky, Physical review letters **122**, 248002 (2019).
[31] M. Pishvar and R. L. Harne, Physical Review Applied **14**, 044034 (2020).
[32] J. N. Chapuis, T. S. Lumpe, and K. Shea, Extreme Mechanics Letters **55**, 101835 (2022).
[33] O. Stenull, C. Kane, and T. Lubensky, Physical review letters **117**, 068001 (2016).

[34] O. R. Bilal, R. Süsstrunk, C. Daraio, and S. D. Huber, Advanced Materials **29**, 1700540 (2017).

[35] G. Baardink, A. Souslov, J. Paulose, and V. Vitelli, Proceedings of the National Academy of Sciences **115**, 489 (2018).

[36] M. Charara, K. Sun, X. Mao, and S. Gonella, Physical Review Applied **16**, 064011 (2021).

[37] M. Charara, J. McInerney, K. Sun, X. Mao, and S. Gonella, Proceedings of the National Academy of Sciences **119**, e2208051119 (2022).

[38] See Supplemental Materials at `URL_will_be_inserted_by_publisher` for details about: the effects of varying the parameter Δ, exploration of the topological polarization of the BK lattice in the ℓ_1, video of experiments, calculations of zero mode decay rates and winding number , $\bar{\gamma}$ BK parametrization and information on its polarization, density calculation, effects of T_h on band diagram, examples of T_d diagonal and T_v vertical mirroring geometries.